Sustainable Structures
ISSN: 2789-3111 (Print); ISSN: 2789-312X (Online)
http://www.sustain-dpl.com/journal/sust
DOI: 10.54113/j.sust.2023.000031

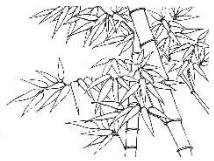

ORIGINAL ARTICLE

Analysis of ultimate fracture bearing capacity of CHS XK-joints welds

Zhenghua Huang [a], Mahmud Ashraf [b], Tao Zheng [a], Yong Yang [a], Enhe Bao [a,*], Han Han [a,*]

[a] School of Civil Engineering, Guizhou University, Guiyang 550025, China
[b]School of Engineering, Deakin University, Geelong Waurn Ponds 3216, Australia.
*Corresponding Author: Enhe Bao, ehbao@gzu.edu.cn, Han Han, 381251345@qq.com

Abstract: The current study presents advanced finite element (FE) models that combine the stress weighted damage model and the crack propagation using explicit dynamic approach of commercial FE software ABAQUS. The applicability of the subroutine for ductile fracture prediction and crack propagation modeling of structural steel is confirmed by comparing the results of fracture tests performed on circumferential notch specimens. FE analysis is performed on 17 circular hollow section (CHS) XK-joint models with various sized partial penetration welds to simulate the fracture process of the joint models, and the obtained results are used to analyze the fracture ultimate bearing capacity of the joint weld. The results indicate that the crack first appears on the inner side of the weld at the crown point of the intersecting line of the tensile web member. The findings also demonstrate that the joint weld does not lose the bearing capacity completely after the initial cracking. Instead, the joint weld's bearing capacity increased with the displacement at the early stages of fracture propagation to reach the maximum value prior to gradual decrease in bearing capacity. A design formula of weld bearing capacity suitable for partial penetration weld has been proposed herein to incorporate the effects of uneven distribution of joint weld stress in the considered XK-joints.

Keywords: Bearing capacity; fracture; partial penetration weld; XK-joints

1 Introduction

The use of long-span steel tubular trusses in various shapes has increased recently due to advanced manufacturing options and emergence of new welding technologies for tubular joints. The steel tube trusses are connected by unstiffened tubular joints, which differ from conventional bolt ball joints and welded ball joints in that they have a concise appearance and a variety of forms [1]. With the increase of use of steel tubular trusses in long-span roof structures, many new types of long-span roof structures adopt the shape of intersecting steel tubular trusses with circular hollow sections (CHS), and the CHS XK-joints have become a common feature at the crossing position, as shown in **Fig. 1**.

In current engineering practice, the design formula used for the weld bearing capacity of an XK-joint is typically the same as that of an X-joint. The design formula for weld bearing capacity is primarily based on X-joints tests. Since multiple branches of spatial XK intersecting nodes are connected at such roof trusses, their possible interactions on the joint stiffness should be tested both experimentally and numerically to determine the suitability of existing design equations for spatial CHS XK-joints.

Received: 24 March 2023; Received in revised form: 4 August 2023; Accepted: 12 August 2023

The fracture failure state of the joint welds in steel building structures often controls their final bearing capacity. The micromechanical model based on the material plastic damage process can represent the influence of the stress-strain field on the internal microstructure characteristics of materials. Such a model can be utilized as a criterion with obvious physical significance to forecast the growth of ductile cracks in steel structural joints more precisely than the standard fracture mechanics technique [2, 3]. The void growth model (VGM) conducted by Rice and Tracey [4] is currently the primary micro mechanism model appropriate for monotonic tensile fracture prediction. The VGM model uses stress triaxiality to characterize the stress state of materials. In recent years, many studies have shown that in addition to stress triaxiality, the Lode angle parameter is also another critical factor affecting plastic flow and ductile failure of metal materials. Smith et al. [5] proposed the stress weighted damage model (SWDM) by introducing the Lode angle parameter based on CVGM model.

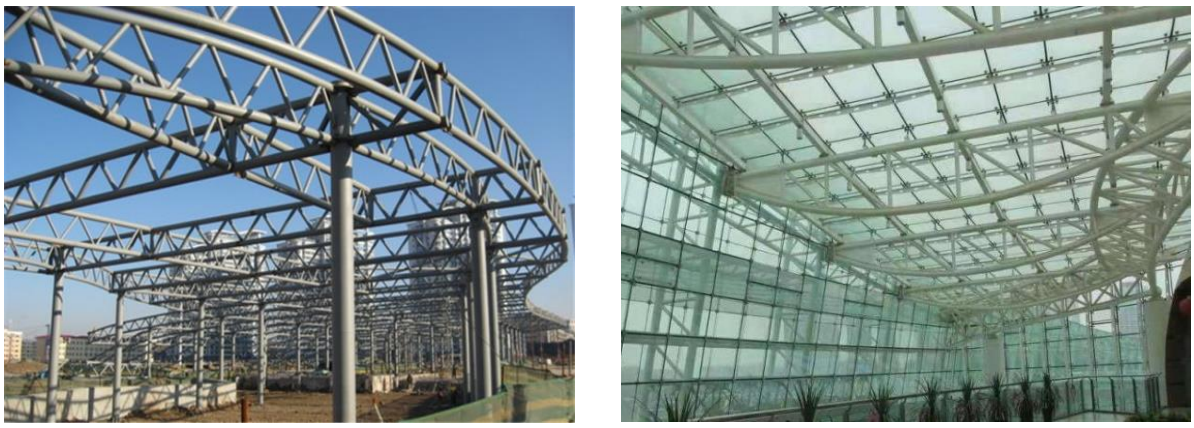

(a) Steel tubular truss at a station building in Jiangshu Province, China

(b) Steel tubular truss at a theater in Henan Province, China

Fig. 1. Cross steel tubular trusses with CHS XK- joints in long-span roof.

Various researchers in relevant fields have studied the ultimate bearing capacity of CHS tubular joints in the fractured state. Wang et al. [6] proposed a damage criterion to predict the macro crack initiation of tubular joints based on continuum damage mechanics. Yin et al. [7] used the VGM and the stress modified critical strain model (SMCS) based on the micro-fracture mechanism to predict the fracture of XK-joints, analyzed the influence of considering the weld configuration in the FE model on the fracture prediction results, and evaluated the importance of considering the weld configuration in the fracture prediction of intersecting joints. Ma et al. [8] studied the failure mode of the X-joint and analyzed the influence of the non-uniformity of stress distribution on the weld strength of the joint by designing the tensile test of six tubular X-joint specimens. Zhao et al. [9] studied the hysteretic behavior of unstiffened circular hollow section (CHS) X-connections subjected to out-of-plane bending moment. Zhao et al. [10] studied the effect of adjacent braces interaction on seismic and static performance of CHS unstiffened tubular connections under out-of-plane bending moment. A series of tests and simulations [11-15] have verified the influence of Lode angle parameters on the prediction accuracy. Therefore, the effect of Lode angle parameters needs to be considered in fracture prediction analysis of tubular joints. Ma et al. [16] conducted monotonic tensile tests on 8 CHS-CHS X-joints and studied the influence of non-uniform stress distribution on the weld bearing capacity of CHS tubular joints and the fracture mechanism by using the triaxiality and Lode angle related fracture model. It was reported that the non-uniform stress distribution has significant influence on the bearing capacity. If the influence of non-uniform stress distribution is ignored, the formula of weld bearing capacity in Chinese code is unsafe [24].

The initial cracking and crack propagation behavior of steel structures affect the failure mode and ultimate bearing capacity of structures. The FE simulation considering crack propagation in the existing literature is mainly realized by ABAQUS user subroutine. Kubǂk et al. [17] developed the user subroutine VUMAT and used ductile fracture criterion incorporated in the commercial FE package ABAQUS to simulate crack growth in a newly designed cylinder with a specified groove. As the ductile fracture criteria could not be directly implemented in ABAQUS, Donghyuk et al. [18] coded a user-defined subroutine called VUSDFLD in FORTRAN to calculate the accumulated damage and

fracture index at the integration point of the high-alloy steel. Ma et al. [19] compiled VUMAT subroutine based on the micro-fracture mechanism and simulated the crack propagation of welded joints through FE software. Similarly, using the VUMAT subroutine, Wang et al. [20] took the VGM model as the criterion and used FE software to track and analyze the post-crack path of two steel tubular column beam flange directly welded joint specimens. Han et al. [21] used the ABAQUS subroutine written into VGM and SWDM fracture prediction model to simulate the fracture failure process of 23 X-joints of orthogonal design. The results showed that by introducing the Lode angle parameter, SWDM can accurately simulate joints' damage accumulation and fracture failure process under different stress states. The prediction accuracy of SWDM models was observed to be higher than that of VGM models.

The weld configuration of tubular CHS joints is complex, and the solid surfaces of welds are spatial curved surfaces. The welds are continuous and smooth along the whole circumference. The tubular CHS joints generally adopt full-circumference fillet welds, full-circumference butt penetration welds, or partial butt penetration welds and partial fillet welds. However, in engineering, it is difficult to place the lining in the branch tubes of the tubular joint during the welding process, and welding slags at the root of butt penetration welds cannot be cleaned. Therefore, the requirement of full penetration is difficult to meet in practice, and hence the butt penetration welds of tubular joints are partial penetration welds. In the technical specification for steel tubular structures (CECS280:2010) [22], it is specified that the weld within 3 mm of the root of the groove does not require full penetration for the welds of the tubular CHS joints, which allows the existence of partial penetration welds.

According to the code for welding of steel structures (GB50661-2011) [23], the effect of incomplete penetration on the effective thickness can be considered by reducing the effective thickness of partial penetration welds. However, the stress concentration at the incomplete penetration tip may significantly affect the fracture bearing capacity of butt welds. To address this issue, the technical specification for steel tubular structures (CECS280: 2010) and the design standard for steel structures (GB50017-2017) [24] have made provisions. These provisions consider the changes in groove angle and gap size of the weld root, as well as the inability to remove or repair welding slag at the weld root of the butt weld. For convenience in the calculation, the connecting weld can be considered as a full-circumference fillet weld, and the adverse effect of incomplete penetration can be conservatively estimated by treating a portion of the fully penetrated weld as a fillet weld. However, this provision mainly applies to partial butt welds and fillet welds. For the case of full-circumference butt penetration welds, even considering the impact of incomplete penetration might be too conservative. In addition, this provision is primarily applicable to planar CHS tubular T, Y, and K-joints, as well as spatial TT-joints and KK-joints. The suitability of such provision for complex spatial CHS tubular joint welds, such as XK-joints and XKT-joints, should be carefully studied.

At present, the bearing capacity of full-circumference full penetration welds, which is essentially the bearing capacity of full-circumference partial penetration welds, experimental research and numerical simulation analysis based on fracture bearing capacity are very limited. Whether the standard calculation formula of weld bearing capacity can be directly used for full-circumference full penetration welds and whether the weld bearing capacity meets the requirements of not less than the joints bearing capacity remains to be studied.

The reference [21] uses the VUSDFLD subroutine embedded in the SWDM model to analyze the fracture propagation process of the CHS X - joints. It compares the FE simulation results with the test results, proving that this analysis method can accurately analyze the fracture process of the CHS tubular joints. Therefore, this paper uses ABAQUS software to conduct FE analysis on the full-circumference partial penetration weld of CHS XK - joints. The simulation of the joint weld fracture process and the tracking analysis of crack propagation path are achieved by incorporating the subroutine of VUSDFLD with the micro-fracture model SWDM. This allows for a more accurate discussion of the fracture ultimate bearing capacity of this type of joint welds, providing a theoretical basis for the calculation, analysis, and engineering application of their fracture bearing capacity.

2. Simulation of fracture propagation based on the microscopic fracture mechanism

2.1 Development of the FE model

In this paper, the FE analyses of 17 CHS XK-joints with partial penetration welds of different sizes were carried out to simulate the fracture process of the joints. There are many intersecting members in the spatial CHS XK -joints, and the stress state of joint welds is complex. The schematic diagram of the joints is shown in **Fig. 2.** In order to facilitate analysis and comparison, the diameter of the chord is 150 mm, the chord wall thickness is 6 mm, and the included angle between the web member axis and the chord axis is 45 degrees. The included angle between the chord axis and strut axis is 90 degrees, the chord length of the FE model is six times the chord diameter, and the length of the strut and web member is four times the maximum diameter of both. The model sizes and geometric parameters are shown in **Table 1**, where parameters D and T are chord member diameter and wall thickness, respectively; parameters d_k and t_k are the web member diameter and wall thickness, respectively; parameters d_x and t_x are the strut member diameter and wall thickness, respectively; parameter β_k is a ratio between d_k and D; parameter β_x is a ratio between d_x and D; γ is a ratio between D and T; a is the gap between two web members.

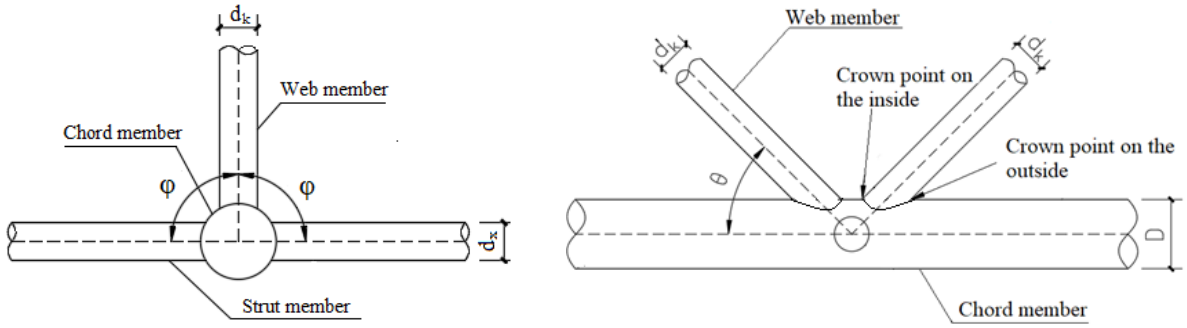

(a) Front elevation (b) Side elevation

Fig. 2. Schematic diagram of the XK circular steel tubular intersecting joint.

The partial penetration welds root gap, b, and blunt edge size of the groove, P, are 0.5 mm and 2 mm, respectively. The weld groove angle of α at the crown points on the inner side of the web member is 60 degrees, and the angel of α at the outside crown points is 22.5 degrees. In all the models, the welds sizes at inner and outer crown points, h_p and h_v, were found to be 6.8 mm and 3 mm, respectively. The welds' effective thickness of h_e at the inner crown point is 2.7 mm, and the welds' effective thickness at the outer crown point is 5.8 mm. The schematic diagram of the welds at the crown points is shown in **Fig. 3**. The weld entity model is shown in **Fig. 4**. The section size of the weld model at the saddle point is shown in **Fig. 5** (h_p =5.5 mm, h_v = 2 mm, and h_e = 2.3 mm).

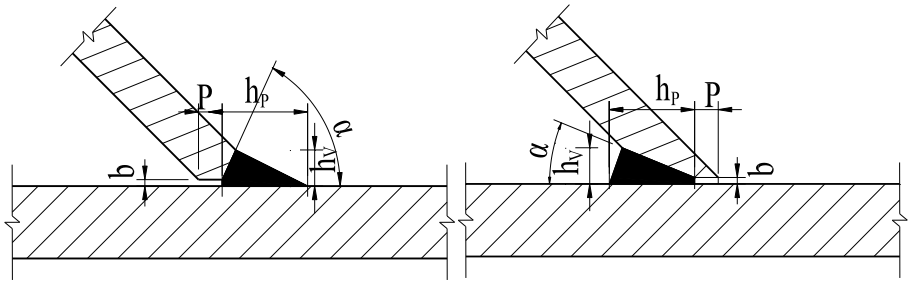

(a) Inner crown point (b) Outer crown point

Fig. 3. Geometric parameters of the crown weld.

The stress state of the chord was not considered, and both ends of the chord were considered fixed. The radial and rotational displacements at the ends of the chord and web member were constrained, and the equivalent tension and compression axial load was applied to the ends of web members. In contrast, the axial tensile load was applied to the strut, which is one-fourths of the load applied to the end of the web member. The models were generated by three-dimensional solid elements, C3D8R. The mesh size of the overall model in the refinement zone was 1.5 mm, while it was 20 mm in the non-refinement zone. The mesh size of the sub-model was no greater than 0.3 mm. Geometric nonlinearity and material

nonlinearity were considered in the FE models. The material model uses the Mises yield surface and isotropic hardening model to simulate the plastic deformation of materials. Because of the symmetry of XK- joints, half of the actual joint was selected for analysis. The overall model and sub-model are shown in **Fig. 6**.

Table 1. Size and geometric parameters of XK-joints models

Specimens	$D\times T$ /mm	$d_k\times t_k$ /mm	$d_x\times t_x$ /mm	β_k	β_x	γ	a/mm
XK-1	150×6	45×4	75×4	0.3	0.5	12.50	20
XK-2	150×6	60×4	75×4	0.4	0.5	12.50	20
XK-3	150×6	75×4	75×4	0.5	0.5	12.50	20
XK-4	150×6	90×4	75×4	0.6	0.5	12.50	20
XK-5	150×6	105×4	75×4	0.7	0.5	12.50	20
XK-6	150×6	75×4	45×4	0.5	0.3	12.50	20
XK-7	150×6	75×4	60×4	0.5	0.4	12.50	20
XK-8	150×6	75×4	90×4	0.5	0.6	12.50	20
XK-9	150×6	75×4	105×4	0.5	0.7	12.50	20
XK-10	150×4	75×4	75×4	0.5	0.5	18.75	20
XK-11	150×5	75×4	75×4	0.5	0.5	15.00	20
XK-12	150×7	75×4	75×4	0.5	0.5	10.71	20
XK-13	150×8	75×4	75×4	0.5	0.5	9.38	20
XK-14	150×6	75×4	75×4	0.5	0.5	12.50	10
XK-15	150×6	75×4	75×4	0.5	0.5	12.50	15
XK-16	150×6	75×4	75×4	0.5	0.5	12.50	25
XK-17	150×6	75×4	75×4	0.5	0.5	12.50	30

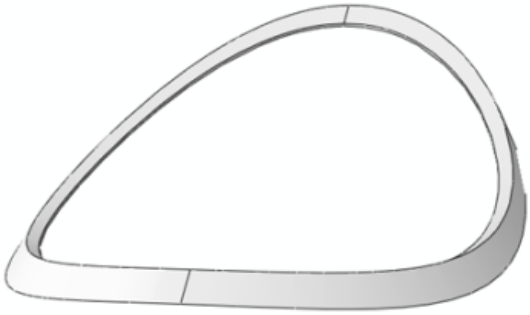

Fig. 4. Weld model.

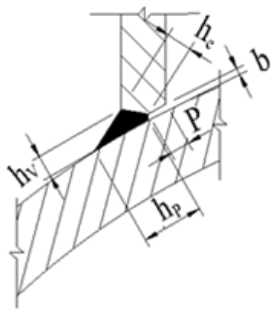

Fig. 5. Geometric parameters of the saddle weld.

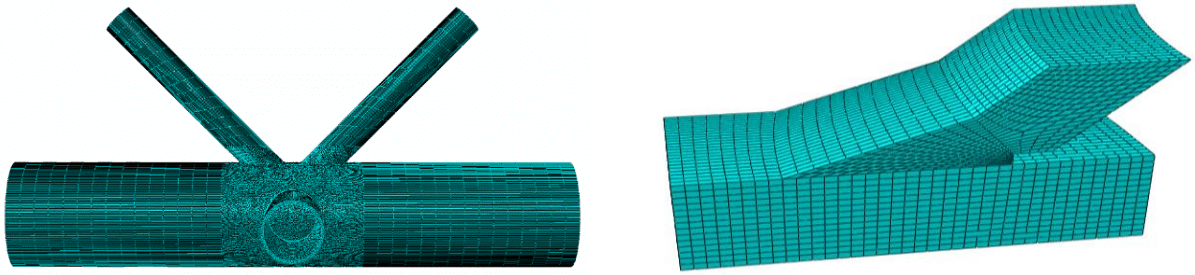

(a) Overall model (b) Sub model

Fig. 6. Finite element model.

2.2 Micro fracture model SWDM and determination of relevant parameters

Based on the CVGM model, Smith et al. [5] considered the damage accumulation problem of components under low-stress triaxiality, and adjusted the fracture model by introducing the variable lode angle parameter to describe the partial stress state and by using a hyperbolic sinusoidal function

instead of the exponential function; and the proposed incremental form of SWDM model is shown in Eq. (1):

$$dD = e^{\lambda\varepsilon_p} C(\beta e^{A+T} - e^{-A-T}) e^{\kappa\xi} d\varepsilon_p \tag{1}$$

Where λ is the cyclic degradation rate, β is the relative rate of damage taken as 1.0, T is the stress triaxiality, test calibration material parameters are C, A+, A- and κ; and ξ is the Lode angle parameter, which can be obtained using Eq. (2):

$$\xi = \cos(3\theta) = \frac{3\sqrt{3}J_3}{2J_2^{1.5}} \tag{2}$$

in which, the value range of ξ is -1 $\leqslant \xi \leqslant$1; And ξ = 1 indicates axisymmetric tensile state, ξ = - 1 indicates axisymmetric compression state, and ξ = 0 indicates plane strain state. In Eq. (2), θ is the lode angle, J_2 is the second invariant of deviatoric stress tensor, and J_3 is the third invariant of deviatoric stress tensor.

The cyclic degradation function is introduced into Eq. (1), which can be used for fracture prediction under cyclic load. Referring to the derivation relationship between VGM model and CVGM model, Eq. (1) is improved to obtain the fracture prediction model under monotonic load [25], and the expression is shown in Eq. (3):

$$dD = Ce^{AT} e^{\kappa\xi} d\varepsilon_p \tag{3}$$

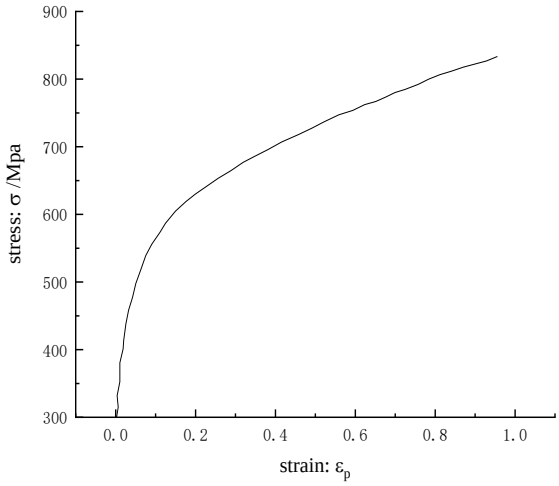

Fig. 7. True stress& plastic strain curve of weld material.

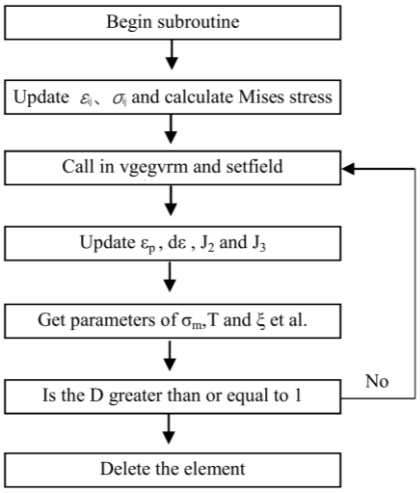

Fig. 8. Flow chart of the subroutine.

Q345 steel is used in the models, and SWDM parameters calibrated by Chen et al [25] are used as the material parameters for the weld material. The elastic modulus E, yield strength f_y, and the ultimate tensile strength f_u were reported to be 209,778 MPa, 358.80 MPa, and 525.43 MPa, respectively. The real stress-plastic strain curve is shown in **Fig. 7**. The micro fracture parameters of the material were set as C = 0.6886, A = 1.1115, and κ = - 0.2779. At present, there are no SWDM parameters of Chinese Q345 steel. It is assumed that the material parameters of steel tubes are the same as those of welds. Since this paper mainly studies weld fracture and considering that the mechanical property parameters of weld material matched with steel tubes are usually similar to the steel tubes, the influence of this assumption on the analysis results can safely be ignored.

2.3 Fracture simulation based on micro fracture mechanism

In this paper, the VUSDFLD subroutine suitable for explicit dynamic analysis is proposed to simulate the fracture process of joints under monotonic load. The SWDM model was compiled into the VUSDFLD subroutine by FORTRAN language. The relevant parameters in the model were specified to be embedded in ABAQUS software to track and analyze the crack propagation path of joints.

VUSDFLD subroutine uses the birth and death element method to delete the elements that reach the fracture criterion in the model. The user needs to specify the number of state variables and the

number of control element variables according to the subroutine. Each time the model is calculated, the state variables of the elements in the model will be updated, and whether the elements in the model meet the ductile fracture level will be determined. If the fracture level is not met, then analysis and calculation of the overall model will continue, or if the fracture criteria is met, the corresponding element will be deleted from the overall model and will not participate in the subsequent analysis and calculation. In this paper, the damage variable *D* of the element is used to judge whether the element meets the ductile fracture standard in the VUSDFLD subroutine: when the damage variable of the element is less than 1, then it is judged that the element does not meet the fracture requirement, or when the damage variable of the element is greater than or equal to 1, the element reaches the fracture requirement. The flow of the VUSDFLD subroutine written in this paper is shown in **Fig. 8**.

2.4 Experimental verification of fracture propagation simulation based on ABAQUS user subroutine

2.4.1 Test overview

Chen Aiguo et al. [25] carried out a series of ductile fracture performance tests on Q345 weld metal. In this section, the aforementioned VUSDFLD subroutine is used to simulate the fracture process of WCNT series specimens with circumferential notch under monotonic load. The accuracy of fracture simulation based on the subprogram is analyzed by comparing the results of the tests and finite element simulations.

The metal material parameters of WCNT series specimens are the same as the aforementioned tubular joints. The total length of the test specimens is 180 mm, the diameter is 10 mm, the length of the gauge section is 40 mm, and the diameter at the notch root is 5 mm. The notch radius of WCNTA specimen is 2 mm, and that of WCNTB specimen is 5 mm. The schematic diagram of WCNTB specimens is shown in **Fig. 9**. The specimens were loaded by an MTS material testing machine, and the elongation was measured by an extensometer during the loading process.

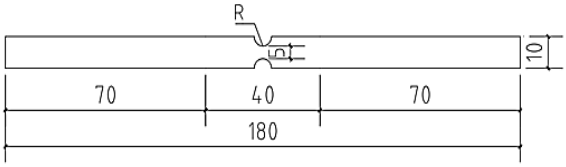

Fig. 9. Schematic diagram of the test specimen. Chen Aiguo et al. [25].

(a) Fracture failure (b) Fracture surface

Fig. 10. Test results of WCNTA. Chen Aiguo et al. [25].

2.4.2 Test results and phenomena

The notch radius of the circumferential notch specimen WCNTA is smaller than that of WCNTB. The change rate of the section area of WCNTA at the notch is greater than that of WCNTB, and hence the stress concentration of WCNTA is more prominent, the hydrostatic stress at the minimum section of the specimen is also more significant, and the deformation capacity of the specimen is relatively weak.

The deformed shape of the circumferential notch specimen WCNTA are shown in **Fig. 10**. The specimen is pulled off from the minimum section of the notch, and the section is cup-shaped.

2.4.3 Results of FE simulation using the subroutine

Fig. 11 shows the results of FE simulation. It can be seen from the figure that before fracture, the stress of the notched section of WCNTA and WCNTB specimens is significantly higher than those of other locations due to the stress concentration effect. The plastic deformation of the notched section was obvious and reached the strengthening stage. The necking phenomenon occurred with load increase, and finally, fracture occurred with the fracture cross sections of WCNTA and WCNTB models were cup-shaped and conical. The simulation results are consistent with the test observations, indicating that the deletion technique used in FE models was suitable for such application. The simulation results using the VUSDFLD subroutine with SWDM criteria are highly consistent with those obtained from test results.

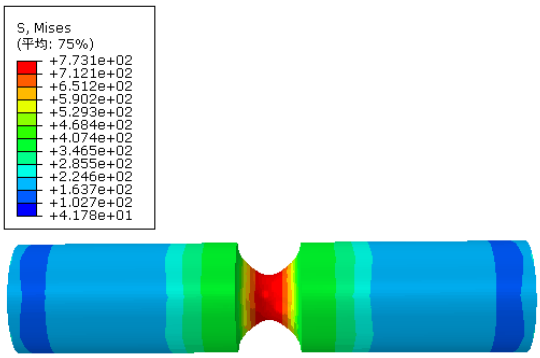

(a) WCNTA stress distribution before fracture

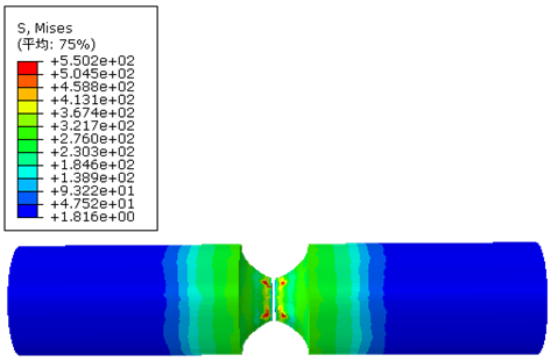

(b) Failure mode of WCNTA

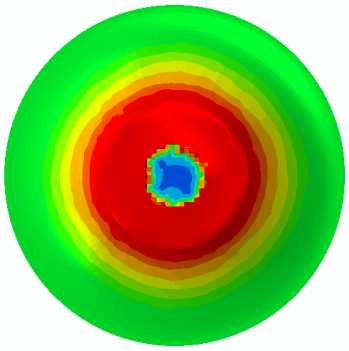

(c) Section fracture extension of WCNTA

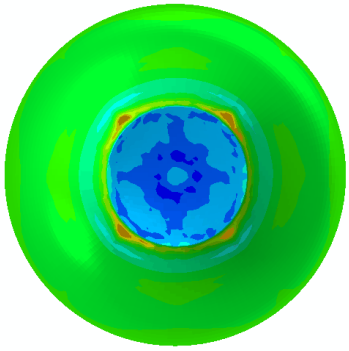

(d) Completely fractured section of WCNTA

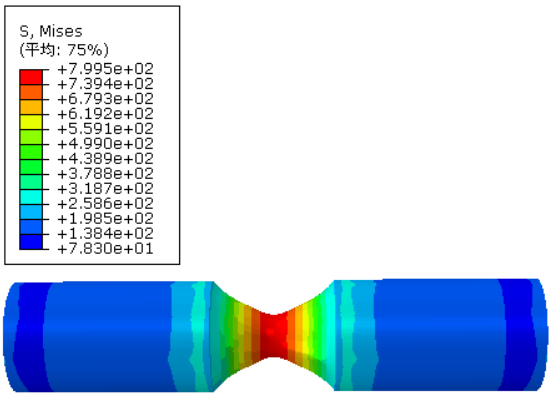

(e) WCNTB stress distribution before fracture

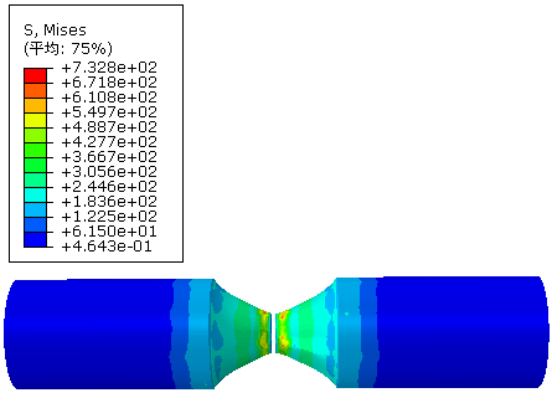

(f) Failure mode of WCNTB

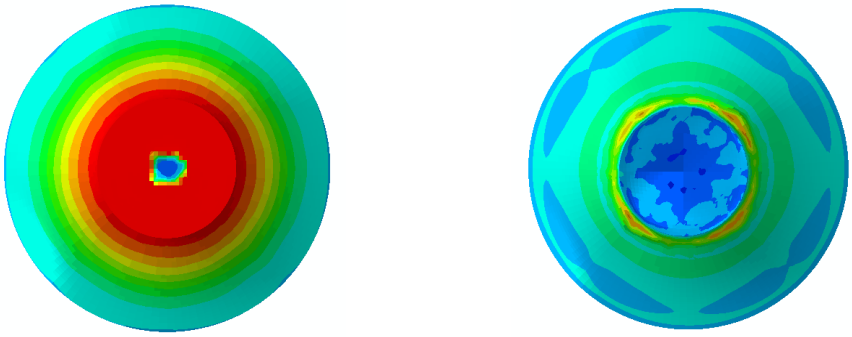

(g) Section fracture extension of WCNTB (h) Completely fractured section of WCNTB

Fig. 11. FE simulation results of test specimens.

The force-elongation curves obtained from the FE models of WCNTA and WCNTB specimens were extracted and compared with those obtained from the tests. The comparison results are shown in **Fig. 12.**

As shown in **Fig. 12**, the force-elongation curves obtained by FE simulation are almost identical to the test curves in the elastic stage, and the degree of agreement is very high in the elastic-plastic to fracture stage. The final fracture load and fracture deformation obtained by test and FE simulation showed minor deviations. These results show that the VUSDFLD subroutine based on the SWDM model can accurately simulate the test process, including the stages of crack initiation, propagation, and complete fracture.

3. Simulation of crack initiation and propagation in CHS-XK joints welds

3.1 Crack initiation prediction of joints

The crack initiation at a joint triggers loss of structural integrity, and it is also considered as an important reference point for studying the bearing capacity of the joint. In the previous FE studies of tubular joints [6-7], the crack initiation of the joints was generally regarded as the failure sign of the joints, but the influence of the fracture process on the joints was not considered. With the continuous increase of the load, the joint reaches the condition of crack initiation resulting in growth of macro cracks. The stress and strain in the joints region will be redistributed in the area that has not been cracked. The cracking area of the joint will lead to more severe stress concentration due to the reduction of the stress area, which will lead to the acceleration of the crack growth rate resulting in a significant decline in the bearing capacity of the joint. Finally, the joint will break entirely and lose its bearing capacity completely. In most cases development of cracks will reduce the bearing capacity of joints but it should be noted that an increase in bearing capacity after crack initiation cannot be completely ruled out as it depends on stress redistribution among connecting elements.

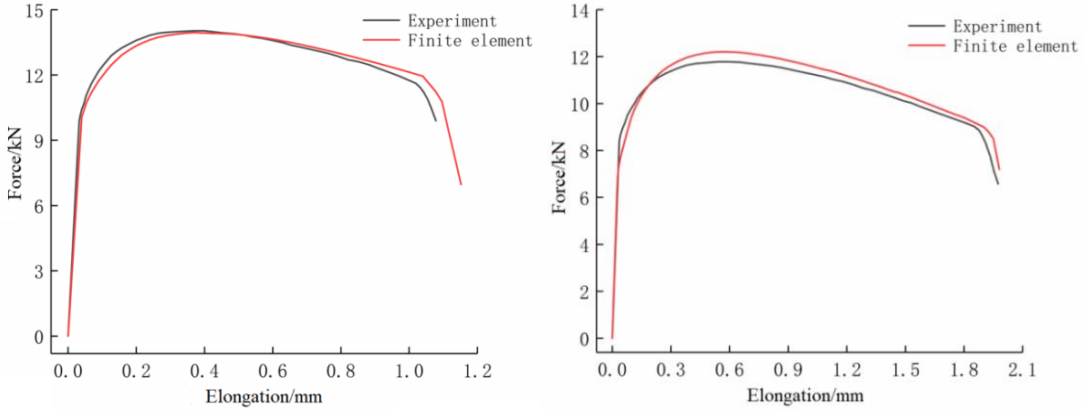

(a) Force-elongation curve of WCNTA (b) Force-elongation curve of WCNTB

Fig. 12. Comparison results of finite element and test.

The VUSDFLD subroutine with SWDM model was embedded in ABAQUS software, and the FE analyses of 17 XK models shown in **Table 1** were carried out by using the dynamic explicit analysis method to simulate their fracture process. The simulation results show that for the joint model in this paper, the non-uniformity of the weld stress distribution is obvious in the whole loading process. The maximum stress point is always at the crown points of the welds of the intersecting line of the tensile web member, and the cracking position of the joint first appears near the crown point on the inside of the weld. Taking model XK-3 as an example, its model cracking diagram is shown in **Fig. 13**.

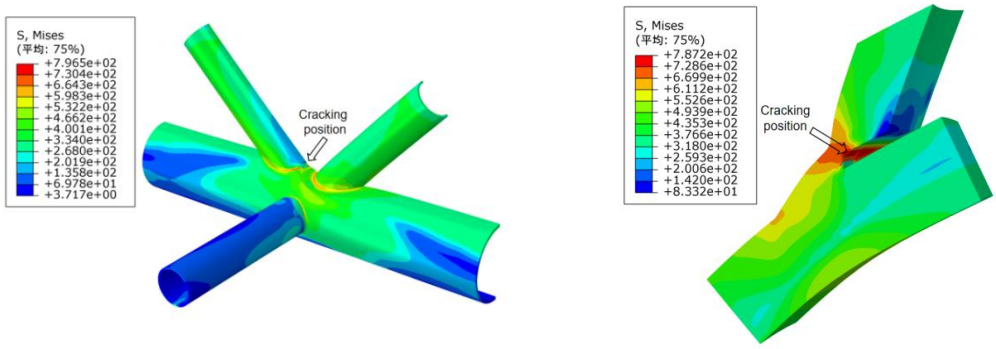

(a) Cracking position (b) Crack initiation point

Fig. 13. Crack formation of model XK-3.

3.2 Fracture propagation simulation of joints

The analysis results showed that when the initial crack occurred in the joint weld at the tension web member, the joint did not lose its bearing capacity immediately; the bearing capacity increased to a certain extent with the expansion of the crack. As the load on the end of the web members and struts continued to increase, the elements satisfying the fracture criterion at the weld crack were deleted from the FE model, and the crack expanded from the crown point to the saddle point along the intersection line with an acceleration in crack growth speed. At the same time, in the weld crack expansion process, the weld's internal stress at the same location is always greater than the external surface under the same load. Therefore, in the direction of the weld thickness, the crack expands from the internal weld's root to the weld's external surface. When the external crack occurred, the internal weld at the same location was completely broken, as shown in **Fig. 14.** Therefore, in practical engineering, it is not possible to find out whether the joint is cracked at the first time. Only when the crack inside the weld extends for a certain extent, the crack on the external surface of the joint weld become visible.

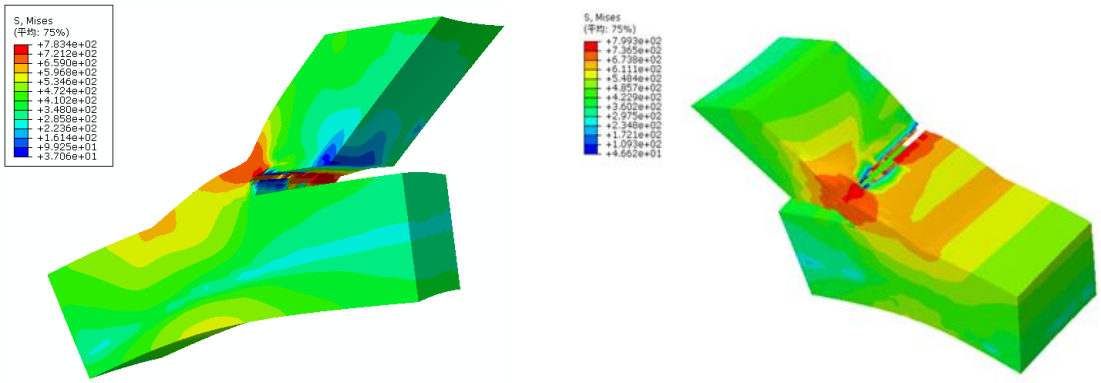

(a) View direction 1 (b) View direction 2

Fig. 14. Schematic diagram of crack propagation.

With the continuous expansion of weld crack, varying degrees of plastic deformation can be found in the steel tube wall at the joint as well as obvious local buckling can be found in tube wall connected to compression web member. The fracture occurs in the joint weld at the tension web. The fracture diagram of the joint model is shown in **Fig. 15**.

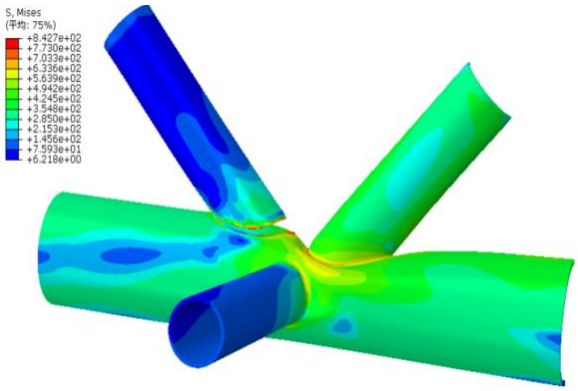

Fig. 15. Fracture diagram of model XK-3.

4. Analysis of the ultimate bearing capacity of welds of XK circular steel tubular joints

4.1 Criteria for ultimate bearing capacity of joint welds

Currently, the ultimate bearing capacity of circular steel tubular joints primarily includes the visible crack criterion, ultimate deformation criterion, and ultimate load criterion [26]. The visible crack criterion refers to the phenomenon when the macroscopic crack appears on the chord wall or connecting weld of the intersecting joint, and then joint is damaged and reaches its ultimate bearing capacity. The visible crack criterion is generally adopted in experimental research. Because the visible situation of the crack depends on the level of the tester, the initial crack occurrence time and its corresponding limit load obtained by different testers will be different in the same test. The ultimate deformation criterion is to control the ultimate bearing capacity of the joint based on the deformation of the joint. With the load increase, the joint's plastic strain increases. The ultimate bearing capacity of the joint is typically reached when the local deformation of the joint reaches a certain threshold. In most cases, this threshold is when the plastic deformation of the chord wall reaches 3% of the chord diameter, as specified in [26]. At this point, it is not advisable to continue loading the joint as it has reached its maximum capacity. Therefore, the load at this stage represents the ultimate bearing capacity of the joint. The ultimate load criterion refers to that when the load-displacement curve of the circular steel tubular joint reaches the peak point and the joint reaches its ultimate bearing capacity.

The ultimate fracture bearing capacity of welds is generally determined according to the visible crack criterion, which is generally used in experimental research. That is, the load when macro cracks occur in the weld is taken as the ultimate load of the weld. In this analysis, the FE software can simulate the process of joint weld cracking and crack propagation through the VUSDFLD subroutine, so the ultimate fracture bearing capacity of the weld can be determined more accurately using the ultimate load criterion.

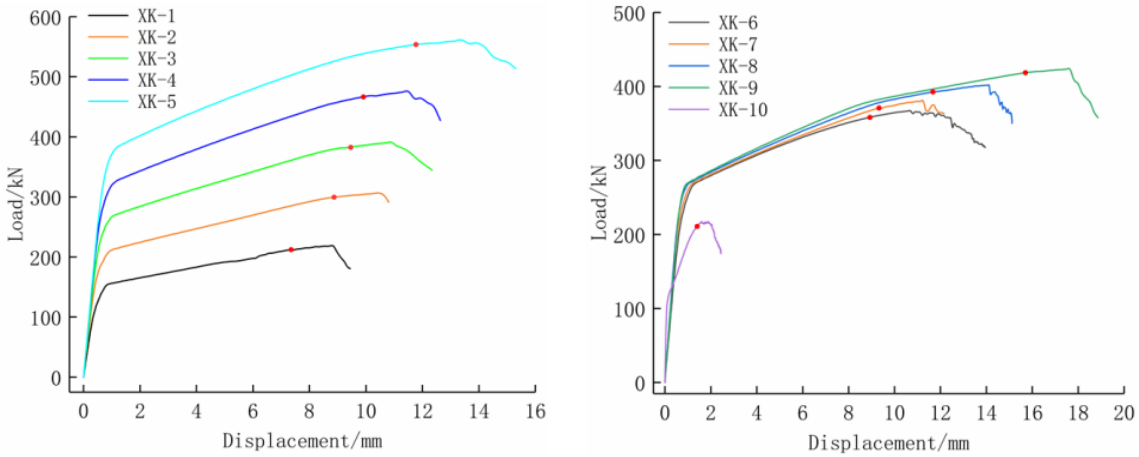

(a) XK-1~XK-5 (b) XK-6~XK-10

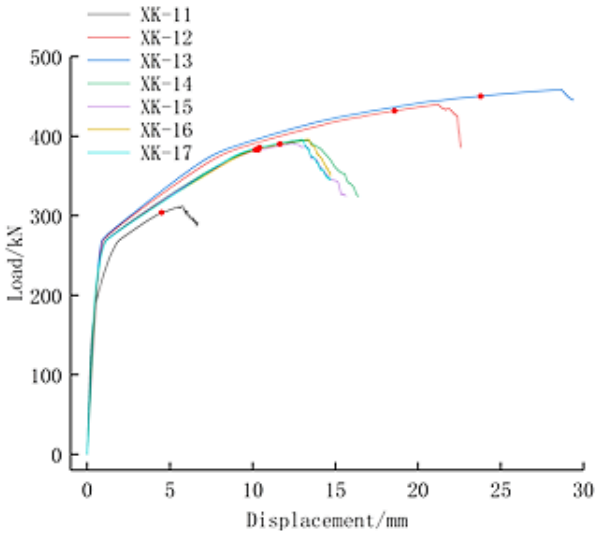

(c) XK11~XK17

Fig. 16. Load-displacement curves obtained from FE models.

The load-displacement curves of 17 FE models were extracted, as shown in **Fig. 16**. The ordinate in the figure is the axial load at the end of the tension web member, and the abscissa is the axial displacement of the tension web member. The red dot on the curve represents the initial cracking point, and the corresponding load and displacement are the initial cracking load and initial cracking displacement, respectively. It can be seen from the diagram that when the load-displacement curve of the joint reaches the cracking point, the curve does not immediately drop. Due to the uneven distribution of weld stress, the stress levels of other welds are relatively low, except for the adjacent area of the cracking point. After cracking, the bearing capacity of the joint weld slightly increases due to the redistribution of stress. The bearing capacity of the joint weld is not reduced or suddenly lost due to cracking, and the bearing capacity of the weld will change with the expansion of the crack. At the initial stage of crack propagation, the joint weld's bearing capacity increases as the displacement increase, and the curve is relatively smooth. When the displacement continues to increase to a certain extent, the curve reaches the peak point, and the corresponding loads are the peak loads. Then, the bearing capacity of the joint weld will decrease as the displacement increase causing an eventual sudden loss showing that the joint has fractured completely. Therefore, according to the provisions of the ultimate strength criterion, it can be considered that the cracking of the joint does not mark that the joint has reached the limit state, the corresponding cracking load is not the ultimate bearing capacity of the joint; instead, the peak load in the curve is the tentative ultimate bearing capacity of the joint. This phenomenon indicates that the ultimate bearing capacity of the joint may occur as the crack propagates. It is worth mentioning that after the load reaches the peak value, the bearing capacity of some joints will not be lost immediately. Still, there will be a declining stage followed by a sudden loss of bearing capacity. At the same time, it can also be found that although the joint can bear greater load after initial cracking, the increased value is in not significant compared to the initial cracking load. It is also feasible to select cracking load as the ultimate bearing capacity from the application perspective.

4.2 Comparison between weld fracture bearing capacity and ultimate bearing capacity of joints

After sorting out the fracture process simulation results of 17 XK model joints, it was found that all joints suffered weld cracking, and no chord wall cracking was observed. The weld fracture bearing capacity N_a is determined according to the ultimate load criterion. The joint ultimate bearing capacity N_b is based on the ultimate deformation criterion, i.e. the corresponding load when the plastic deformation of the chord wall reaches 3% (4.5 mm) of the chord diameter. The fracture bearing capacity and the ultimate bearing capacity of joint are compared in Table 2. The parameter h_{em} is the average of the effective thickness of each feature point weld, while ΔN_{ab} is the difference between joint ultimate bearing capacity N_b and weld fracture bearing capacity N_a.

Table 2. Comparison between weld fracture ultimate bearing capacity and ultimate bearing capacity of joints

Models	N_a/kN	N_b/kN	ΔN_{ab}/kN	h_{em}/T	$\Delta N_{ab}/N_b$
XK-1	218.56	177.13	41.43	0.60	0.23
XK-2	309.82	246.25	63.57	0.60	0.26
XK-3	390.70	329.49	61.21	0.60	0.19
XK-4	475.56	418.27	57.29	0.60	0.14
XK-5	561.30	545.62	15.68	0.60	0.03
XK-6	370.43	310.32	56.76	0.60	0.18
XK-7	380.48	321.71	58.77	0.60	0.18
XK-8	401.65	360.34	41.31	0.60	0.11
XK-9	423.16	397.42	25.74	0.60	0.06
XK-10	217.33	130.86	57.15	0.90	0.36
XK-11	311.61	235.63	75.98	0.72	0.32
XK-12	439.97	-	-	0.51	-
XK-13	457.87	-	-	0.45	-
XK-14	394.63	391.72	2.91	0.60	0.01
XK-15	390.83	318.80	72.03	0.60	0.23
XK-16	393.04	329.25	66.79	0.60	0.20
XK-17	395.96	309.83	86.13	0.60	0.28

As listed in **Table 2**, for most joint models except XK-12 and XK-13, the weld fracture bearing capacity N_a was greater than the joint ultimate bearing capacity N_b, and the chord wall thickness of these joints is not more than 6 mm. The difference between N_a and N_b is denoted as ΔN_{ab}, and the maximum and minimum values of ΔN_{ab} are 86.13 kN and 2.91 kN, respectively. The ratio of ΔN_{ab} to N_b is 0.36 at the maximum and 0.01 at the minimum. That is to say, in the models listed in **Table 2**, the ultimate fracture bearing capacity of the weld of each model is larger than the ultimate bearing capacity based on the ultimate deformation criterion, and the difference range is from 1% to 36%. This shows that the ultimate bearing capacity of these joints is not controlled by the fracture strength of the weld but by the deformation. The fracture bearing capacity of the weld is not less than the bearing capacity based on the ultimate deformation criterion, which meets the requirements of the Chinese steel structure standard (GB50017-2017). For most of these joint models, the weld size h_p of the weld is larger than the chord wall thickness.

For joints XK-12 and XK-13, the chord thickness is larger than other model joints, which are 7 mm and 8 mm, respectively, so the stiffness of the chord wall is larger. Therefore, the weld will fracture completely when the plastic deformation of the chord wall has not yet reached 3% of the chord diameter. Then the fracture bearing capacity of the weld cannot meet the requirements larger than the joints' ultimate bearing capacity. It can be found that in all analysis models, only XK-12 and XK-13 chord wall thickness exceeds the weld size h_p, and only in these two models the fracture bearing capacity of the weld is less than the ultimate bearing capacity determined according to the ultimate deformation criterion.

It can be inferred that for XK circular steel tubular joints with partial penetration welds, when the weld size h_p is relatively small compared to the chord wall thickness (the weld size h_p of the models listed in **Table 2** are all less than the chord wall thickness), the fracture bearing capacity of the weld may be less than the bearing capacity of the joint, which does not meet the requirements of Chinese steel structure standard (GB50017-2017).

4.3 Calculation method of bearing capacity of joint welds

According to the Chinese steel structure standard, when the web member of circular steel tubular joint is only subjected to axial force, the design value of bearing capacity of a full circumference fillet weld is

$$N_f = 0.7 h_f l_w f_f^w \tag{4}$$

Where l_w is the calculated weld length, f_f^w is the design value of fillet weld strength, and h_f is the fillet size of fillet weld. This calculation formula is applicable in most cases. Still, some studies have

shown that [19], for the tubular joints with full circumference fillet welds, the weld stress distribution of some geometric parameter nodes is uneven, and the above formula may lead to unsafe results. The research in literature [19] also shows that with the increase of the diameter-thickness ratio of the chord, the unevenness of the weld stress increases as the average fracture strength of the weld decreases, and this formula is not suitable for tubular joints with large diameter-thickness ratio.

Eq. (5) only applies to the case of full circumference fillet weld or partial fillet weld and partial butt weld. For the case of full circumference partial penetration weld, based on the assumption of uniform stress on the whole length of the weld, the average of the effective thickness of the crown point and saddle point weld is taken as the nominal average effective thickness of the weld, which is denoted as h_{em}. With the average of the effective thickness h_{em} replaces $0.7h_{\mathrm{f}}$ in Eq. (5), and then using the design strength of penetration weld $f_{\mathrm{t}}^{\mathrm{w}}$ replaces the design strength of fillet weld $f_{\mathrm{f}}^{\mathrm{w}}$, the design equation of weld bearing capacity of full circumference partial penetration weld can be expressed as

$$N_{\mathrm{f}} = h_{\mathrm{em}} l_{\mathrm{w}} f_{\mathrm{t}}^{\mathrm{w}} \tag{5}$$

The weld bearing capacity of 17 XK model joints is calculated using the aforementioned equation and compared with the weld fracture bearing capacity determined by numerical simulation, as shown in **Table 3**. According to the Chinese steel structure design standard, the design value of the penetration weld strength is equal to the yield strength of the weld (358.8 MPa) divided by the partial factor for resistance (1.087), we get the design strength of the penetration weld $f_{\mathrm{t}}^{\mathrm{w}}$ =330.08 MPa. The applicability of Eq. (6) is evaluated by using the average fracture strength of weld fracture and comparing it with the design strength of the weld. Replace N_f with the fracture bearing capacity of the weld in Eq. (6) to obtain the actual average fracture strength of the weld as follows

$$f_{\mathrm{f,m}} = N_{\mathrm{a}} / (h_{\mathrm{em}} l_{\mathrm{w}}) \tag{6}$$

Table 3 contains a list of each model's computation outcomes. As can be seen, the ratio between the average fracture strength of the weld and the design value of weld strength ranges from 0.70 to 1.47, denoted as weld fracture stress ratio ρ. The ratios of models X10 and X11, 0.70 and 1.00, respectively, are the smallest. Other models' ratios range from 1.13 to 1.47 and are comparatively steady.

The different values of weld fracture stress ratio ρ demonstrate that the average fracture strength of the weld is also highly varied since the geometric parameters of each joint model simulated in this research are not the same, leading to a significant variance in the ratio of the anticipated fracture load to the typical design value of Eq. (6). The stress and strain distribution of the joint weld under load is not uniform due to the influence of the stress concentration brought on by the irregular geometric shape, and the average fracture strength of the weld is closely correlated with the level of non-uniformity of the stress and strain distribution. The fracture bearing capacity and average fracture strength of a matching weld are inversely correlated with the degree of unevenness in the weld's stress distribution.

Table 3. Simulation results of joint models

Models	l_{w}/mm	h_{em}	β_k	γ	N_{f}/kN	N_{a}/kN	$f_{f,m}$/MPa	$f_{f,m}/f_t^w$
XK-1	171	3.4	0.3	12.50	193.60	218.56	372.63	1.13
XK-2	230	3.4	0.4	12.50	255.09	309.82	400.91	1.21
XK-3	288	3.3	0.5	12.50	311.81	390.70	413.60	1.25
XK-4	347	3.2	0.6	12.50	367.67	475.56	426.94	1.29
XK-5	405	3.1	0.7	12.50	415.75	561.30	445.64	1.35
XK-6	288	3.3	0.5	12.50	313.71	370.43	389.76	1.18
XK-7	288	3.3	0.5	12.50	311.81	380.48	402.78	1.22
XK-8	288	3.3	0.5	12.50	311.81	401.65	425.19	1.29
XK-9	288	3.3	0.5	12.50	311.81	423.16	447.96	1.36
XK-10	288	3.3	0.5	18.75	311.81	217.33	230.07	0.70
XK-11	288	3.3	0.5	15.00	311.81	311.61	329.87	1.00
XK-12	288	3.3	0.5	10.71	311.81	439.97	465.75	1.41
XK-13	288	3.3	0.5	9.38	311.81	457.87	484.70	1.47
XK-14	288	3.3	0.5	12.50	311.81	394.63	417.76	1.27
XK-15	288	3.3	0.5	12.50	311.81	390.83	413.73	1.25
XK-16	288	3.3	0.5	12.50	311.81	393.04	416.07	1.26
XK-17	288	3.3	0.5	12.50	311.81	395.96	419.16	1.27

Fig. 17 depicts the maximal equivalent Mises stress at each characteristic weld position at the time of cracking for each model, where 0 °is the inner crown point, 180 °is the outer crown point, and 90 °is the saddle point. The figure shows how each characteristic weld point's maximal equivalent Mises stress value fluctuates according to the geometric model parameters.

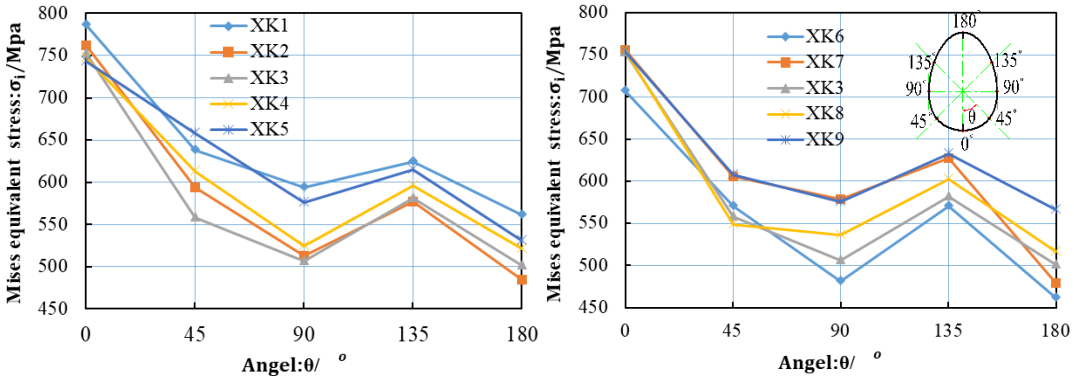

(a) Change with β_k (b) Change with β_x

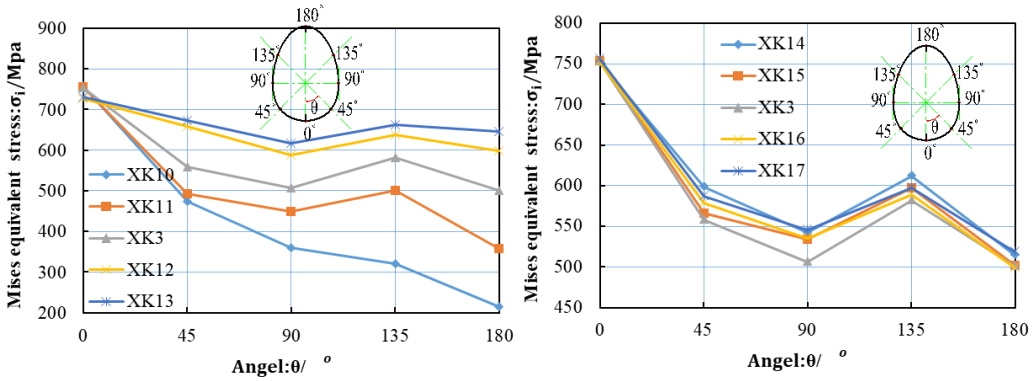

(c) Change with γ (d) Change with a

Fig. 17. Characteristic points Maximum Mises stress distribution of models weld

Fig. 17 a shows model XK1 to XK5, in which the geometric parameters β_k increases from 0.3 to 0.7, and the other parameters remain unchanged. **Fig. 17 b** shows XK6 to XK9, in which the geometric parameters β_x increases from 0.3 to 0.7, and other parameters remain unchanged. **Fig. 17 c** shows XK10 to XK13, in which the geometric parameters γ reduced from 18.75 to 9.38, and the other parameters remain unchanged. **Fig. 17 d** shows XK14-XK17, in which the geometric parameters a increased from 10 mm to 30 mm. It can be seen from the figure that the Mises stress distribution at different characteristic points of the weld at the moment of cracking has different degrees according to different geometric parameters. The parameters γ have a great influence on the stress distribution, the parameters β_k and β_x have a certain influence on the stress distribution, while the parameters a has little influence on the stress distribution.

The stress uniformity coefficient η is used to evaluate the stress uniformity during weld cracking, which is defined as

$$\eta = \sigma_m / \sigma_c \tag{7}$$

Where σ_m is the average value of the maximum Mises stress at crown points, saddle points ,and 45 ° points in **Fig. 17**, σ_c is the maximal Mises stress at the inner crown point. Therefore the larger the stress uniformity coefficient η, the closer the maximum Mises stress at each position. When the stress uniformity coefficient η= 1, which means that the maximum Mises stress at each position is equal, and the stress distribution is the most average; When the stress uniformity coefficient η=1/8, which means that the maximum Mises stress at all positions except the medial crown point is zero, and the non-uniformity of the stress distribution is largest in theory.

Considering that the maximum equivalent Mises stress at the inner crown point of all models has little difference when cracking, so when the difference between the maximum equivalent Mises stress values at each characteristic point is smaller, that is, the greater the stress uniformity coefficient η,the higher the value of weld fracture stress ratio ρ. The weld fracture stress ratio ρ and stress uniformity coefficient η have a positive correlation, and assuming weld fracture stress ratio ρ is only related to stress uniformity coefficient η, and the 17 models data of ρ and η are extracted for linear regression analysis, **Fig. 18**. The generated linear regression equation has a correlation coefficient of r = 0.93 and a judgment coefficient of R^2 = 0.87, indicating a good correlation between stress uniformity variable η and weld fracture stress ratio ρ and a high degree of linear regression equation fitting, which can be taken to postulate that weld fracture stress ratio ρ is only related to stress uniformity coefficient η.

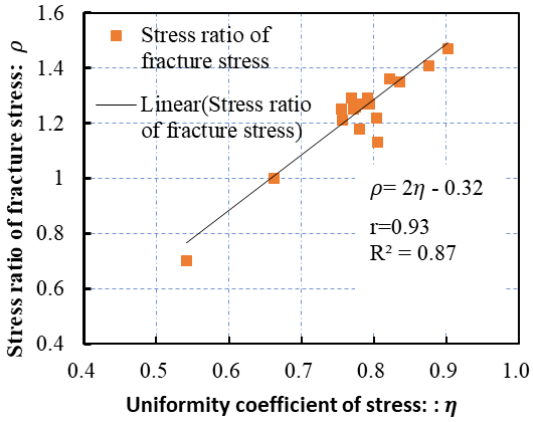

Fig. 18. Correlation between ρ and η.

Fig. 19 shows the curve of weld fracture stress ratio ρ with the geometric parameters of the joints, in which parameter γ has a significant influence on ρ, parameters β_k and β_x have a certain influence on ρ, while parameter a has little influence on ρ. **Fig. 19** also shows the variation curve of $\eta$with the geometric parameters of the models. It can be seen from the figure that the parameter γ has a significant influence on the stress uniformity coefficient η, parameters β_k and β_x have a small and irregular influence on η. In contrast, parameter a's influence is very small and can be ignored.

Seventeen models' fracture stress ratio η and joint geometry parameters are analyzed by linear regression, and the results are shown in **Table 4. Fig. 20** displays the regression analysis findings for the fracture stress ratio η and parameter geometry lg(γ), which reveals that the linear regression correlation coefficient r is 0.93 and the judgment coefficient R^2 is 0.87. It demonstrates that lg(γ) and η have a strong association, and the linear regression equation fits the data well. Similarly, linear regression was used to analyze the other three groups of model analysis data (η and β_k, η and β_x, as well as η and a). The linear correlation coefficients r for the three data groups are 0.21, 0.046, and 0.018, respectively. The determination coefficients R^2 are 0.044, 0.0022, and 0.00033, which indicates that η has little correlation with parameters β_k, β_x, and a. Therefore, parameter η can be assumed only related to lg(γ).

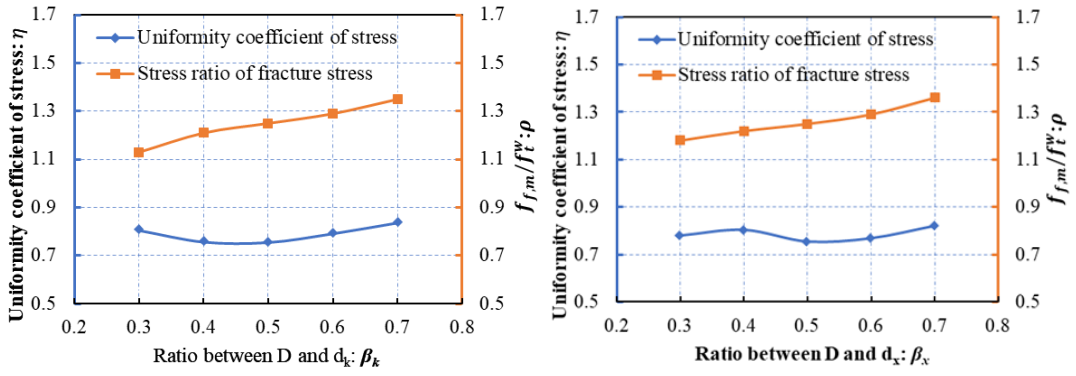

(a) Change with β_k (b) Change with β_x

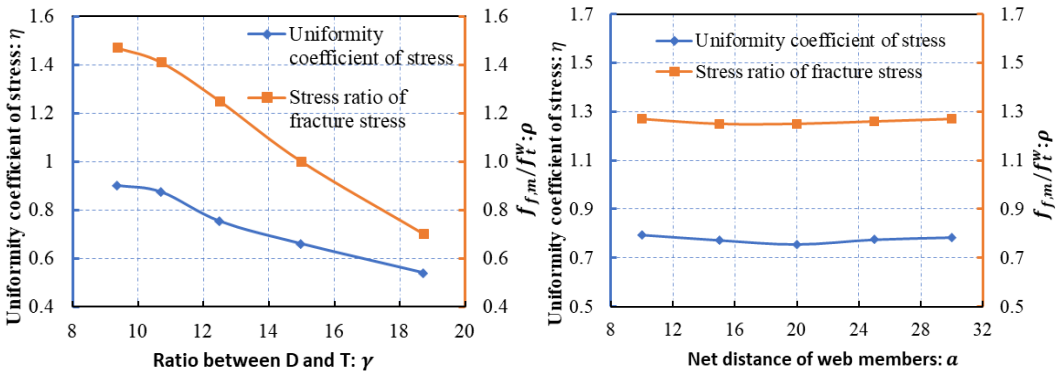

(c) Change with γ (d) Change with a

Fig. 19. Relationship curves between geometric parameters and both η and ρ.

Table 4. Linear regression analysis of geometric parameters

regression variable	r	R^2	standard error
η& lg(γ)	0.95	0.90	0.025
η&β_k	0.21	0.044	0.076
η&β_x	0.046	0.0022	0.078
η&a	0.018	3.3×10^{-4}	0.078

The linear regression equations for ρ and η are determined by regression analysis of two groups' analysis data (ρ and η, η and lg(γ)), and they are as follows:

$$\begin{cases} \rho = 2\eta - 0.32 \\ \eta = -1.27\lg(\gamma) + 2.18 \end{cases} \tag{8}$$

Where, according to the physical meaning of the parameter, it shall meet $0.16<\eta< 1$, $0<\rho<1.57$, corresponding γ range from 8.5 to 39, and due to the regression data of γ range actually from 9.38 to 18.75, so parameter γ in these equations range from 9.38 to 18.75.

The partial coefficient of resistance of weld bearing capacity, denoted as γ_R, is the ratio of the weld's actual bearing capacity to its design value. The uniform stress presumption of formula (6) dictates that γ_R should have a constant value. The partial coefficient of resistance γ_R of the butt weld strength of Q355 steel (E50) is 1.574, as stated in GB 50017-2017. However, as the investigation in this paper shows that the stress uniformity coefficient affects the actual average fracture strength, the calculation formula for the actual value of γ_R is

$$\gamma_R = \frac{N_a}{N_f} = f_{f,m} / f_t^w = \rho \tag{9}$$

The above equation shows that the essence of ρ is the partial factor of resistance. Because ρ changes with different diameter thickness ratios γ, the partial coefficient of resistance of formula (10) is not a constant, which will lead to the reliability level of the design value of weld bearing capacity of different joints is very different or even unsafe. To avoid this situation, it is necessary to modify the design value of weld bearing capacity in formula (6), which is defined as

$$N_f = \alpha h_{em} l_w f_t^w \tag{10}$$

Where α is the adjustment factor to offset the impact of the non-constant value of weld fracture stress ratio ρ. Substitute the Eq.10 into Eq. 9, we get the new calculate formula of γ_R as shown in Eq. (11).

$$\gamma_R = \frac{N_a}{N_f} = f_{f,m} / f_t^w / \alpha = \rho / \alpha \tag{11}$$

When η= 1, the completely uniform stress state, is substituted into Eq. (9), we get ρ= 1.68, nearly identical to the resistance partial coefficient of 1.57 determined by GB 50017-2017 for butt weld

strength. To obtain a constant reliability close to that determined by the Chinese code equations. The γ_R is defined as the resistance partial factor under completely uniform stress, i.e. γ_R =1.68, and then substituting it into Eq. (11) will yield Eq. (12).

$$\alpha = 0.6\rho \tag{12}$$

Then substituting Eq.(12) into Eq.(10), we get the modified equation Eq.(13), which may be used to calculate the design value of the bearing capacity of full circumference partial penetration welds with constant partial resistance coefficients of 1.68.

$$N_f = 0.6\rho h_{em} l_w f_t^w \tag{13}$$

The parameters meaning in Eq. (13) is the same as mentioned above. It should be noted that when calculating the nominal average effective thickness h_{em} of the weld, the effective thickness h_e of each feature point is the actual effective thickness of the weld, which does not take into account the reduction of the thickness in the actual project due to the failure of slag removal and repair welding of partial penetration welds. Therefore, when applying this formula in practical engineering, the effective thickness h_e should be reduced according to the actual situation or the provisions of relevant specifications. For example, the effective thickness h_e can be reduced by referring to the corresponding provisions of article 5.3.4 of the China code for welding of steel structures (GB50661-2011).

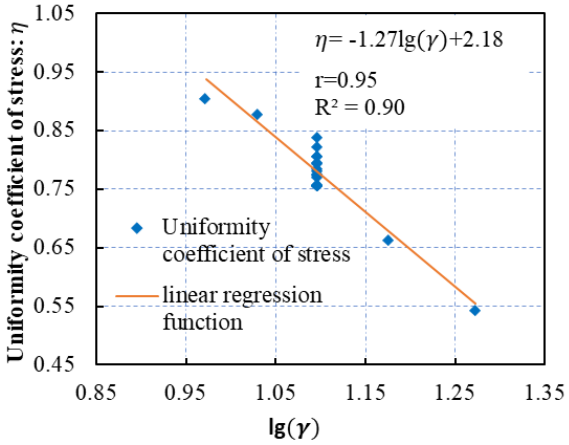

Fig. 20. Linear regression of η&lg(γ).

4.4 Calculation examples of joint weld bearing capacity

Based on the VUSDFLD subroutine, the finite element analysis of the fracture ultimate bearing capacity of two circular steel tubular XK-joints of the same type as the models in the previous section is carried out. The specific geometric dimensions of the example model are shown in **Table 5**. The example model adopts partial penetration weld, and its weld shape is the same as in **Fig. 3**- **Fig. 5**. The values of b, P, and α are identical to the models in Table 1. The weld sizes of the inner and outer crown point weld are equal to h_p=10 mm and h_v=4.5 mm. The inner crown point butt weld's effective thickness is h_e=4.6 mm, and the outer crown point weld's effective thickness is h_e=8.7 mm. The effective thickness of the saddle point of XK-S1 is h_e=5.0 mm, and the effective thickness of the saddle point of XK-S2 is h_e=4.8 mm. The average effective weld thickness of XK-S1 and XK-S2 is calculated to be 5.8 mm and 5.7 mm, respectively, based on the effective weld thickness data of crown points and saddle points.

Then, for the two example models, Eq. (6) without considering the non-uniformity of weld stress and Eq.14 considering the influence of non-uniformity of stress are used to calculate the design bearing capacity of weld, respectively. The analysis results of the model example are shown in **Table 6**, where N_f' is the weld bearing capacity calculated by Eq. (14) and N_f is the weld bearing capacity calculated by Eq. (6). **Table 6** shows that the weld bearing capacity N_f obtained without taking into account the influence of weld stress heterogeneity is relatively larger, and the ratio of the ultimate fracture bearing capacity to the design bearing capacity derived by Eq.6, that is, the resistance analysis coefficient of the weld, is 1.17 and 0.87 respectively, which is much less than the resistance partial coefficient provided in

the Chinese specification (GB 50017-2017). The design bearing capacity calculated by Eq. (6) is larger than the actual fracture ultimate bearing capacity, particularly for model XK-S2, whose resistance partial coefficient is smaller than 1.

Table 5. Dimension and geometric parameters of example XK joint models

Example models	D* T /mm	d_k *t_k /mm	d_x *t_x /mm	β_k	β_x	γ	a/mm
XK-S1	225*9	90*6	113*6	0.4	0.5	12.50	20
XK-S2	225*6	113*6	113*6	0.5	0.5	18.75	20

Therefore, applying Eq.6 of the uniform stress assumption in the design process will considerably increase the likelihood that joint welds will fail under the design load and even lead to significant consequences from fracture failure. Using the recommended weld design bearing capacity Eq. (14) and accounting for weld stress non-uniformity, the resistance partial factors are 1.56 and 1.87, respectively, slightly different from the specification's weld strength resistance partial factor of 1.57.

Through the analysis and comparison of numerical examples, using Eq. (14) proposed in this paper, which takes into account the uneven effect of weld stress, can not only avoid the situation where the design bearing capacity is larger than the actual ultimate fracture bearing capacity, but also make the failure probability of this type of joint welds of different sizes tend to be roughly stable under the action of design load, and with a safety degree that is close to and meets the requirements of the design specification.

Table 6. Simulation results of example XK joint models

Example models	l_w /mm	γ	η	ρ	h_{em}	N_f'/kN Eq.(14)	N_f/kN	N_a/kN Eq.(6)	N_a/N_f	N_a/N_f'
XK-S1	345	12.50	0.79	1.25	5.8	495.37	660.50	773.44	1.17	1.56
XK-S2	442	18.75	0.56	0.81	5.7	404.16	831.60	720.42	0.87	1.78

5. Conclusion

17 tubular XK-joint models were carefully investigated using FE modelling technique and it was observed that the fracture of the partial penetration weld occurred at the root of the tension web member. By embedding the subroutine of VUSDFLD with micro fracture model SWDM, the simulation of the joints weld fracture process and the tracking analysis of crack propagation path were captured, and the fracture bearing capacity of this type of joint weld could be evaluated more accurately. The fracture bearing capacity and fracture displacement increased relative to the initial cracking moment, considering the impact of the crack propagation. The final fracture bearing capacity did not increase significantly, but the ultimate fracture displacement was significantly greater than the cracking displacement.

The Chinese code requirements state that the weld's fracture bearing capacity must be greater than the joint's bearing capacity. However, this requirement may not be met when the weld size (h_p) for circular tubular XK-joints with partial penetration welds is smaller than the chord wall thickness. To identify the minimum weld size requirements that comply with the requirements of the code regulations, more testing and numerical simulation analyses must be conducted subsequently.

The unequal stress distribution of the joint weld is not considered by the existing Chinese code formula, which causes significant variation in the resistance partial coefficients of the design values of the weld bearing capacity of various geometric parameters. The formula's calculation results for XK-joints with large diameter thickness ratios will be unsafe. This problem can be avoided by using the calculation formula suggested in this study, which appropriately considers the impact of uneven stress distribution. The range and quantity of regression model parameters impact the linear regression calculation formula for fracture average strength and stress uniformity coefficient, which limits its applicability. The range of model parameters should be increased in the future to broaden its application.

The effective thickness of the weld in the calculation formula for the design value of bearing capacity suggested in this work is the actual effective thickness in the finite element model, which does

not take into account the reduction of thickness owing to the failure of slag removal and repair welding of some full penetration welds. These influencing factors must be taken into account when determining the real effective thickness in practical engineering, and its effective thickness should be reduced.

Funding Statement

The research presented in this paper was supported by the Natural Science Foundation of China (NSFC) through Grant No.51368009 and was also supported by the Natural Science Foundation of Guizhou province (CN) through Grant No. (2018) 1036.

CRediT authorship contribution statement

Zhenghua Huang: Investigation, Supervision, conceptualization, Funding acquisition, writing—original draft preparation. **Mahmud Ashraf**: Supervision, Writing – review & editing. **Tao Zheng**: Supervision, conceptualization. **Enhe Bao**: Supervision, Investigation, conceptualization. **Han Han**: Formal analysis, writing—original draft preparation. **Yong Yang**: Formal analysis, Writing – editing.

Conflicts of Interest

The authors declare that they have no conflicts of interest to report regarding the present study.

References

[1] Broniewicz M, Broniewicz F. Welds Assessment in K-Type Joints of Hollow Section Trusses with I or H Section Chords. Buildings 2020; 10(3): 43. https://doi.org/10.3390/buildings10030043.

[2] Xue L. A unified expression for low cycle fatigue and extremely low cycle fatigue and its implication for m onotonic loading. Fatigue 2008; 30(10-11): 1691-1698. https://doi.org/10.1016/j.ijfatigue.2008.03.004.

[3] Hancock JW, Mackenzie AC. On the mechanisms of ductile failure in high-strength steels subjected to mult i-axial stress-states. Mech. Phys. Solids 1976; 24(3): 147-160. https://doi.org/10.1016/0022-5096(76)90024 -7.

[4] Rice JR, Tracey DM. On the ductile enlargement of voids in triaxial stress fields. Mech. Phys. Solids 1969; 17(3): 201-217. https://doi.org/10.1016/0022-5096(69)90033-7.

[5] Smith CM, Deierlein GG, Kanvinde AM. A stress-weighted damage model for ductile fracture initiation in structural steel under cyclic loading and generalized stress states. CA: Stanford University, 2014:161-244.

[6] Wang B, Hu N, Kurobane, Y, Makino Y, Lie ST. Damage criterion and safety assessment approach to tubular joints. Eng. Struct.2000; 22(5): 424-434. https://doi.org/10.1016/S0141-0296(98)00134-5.

[7] Yin Y, Che XY, Han QH, Lei P. Study on ultimate load bearing capacity of tubular XK-joints based on micr omechanical fracture models. China. J. Civil. Eng.2017; 50(7): 20-26+121. https://doi.org/10.15951/j.tmgc xb.2017.07.003. (in Chinese).

[8] Ma X, Wang, W, Chen, Y. Experiment and mechanism analysis of weld fracture of orthogonal CHS-CHS X-joint. Build. Struct.2018; 39: 139-148. https://doi.org/ 10.14006/j.jzjgxb.2018.03.017.

[9] Zhao BD, Fang C, Wang W, Cai YZ, Zheng YN. Seismic performance of CHS X-connections under out-of-plane bending. J. Constr. Steel Res. 2019; 158: 591–603. https://doi.org/10.1016/j.jcsr.2019.04.019.

[10] Zhao BD, Sun C, Zheng YN, Cai YZ. Effects of adjacent brace interaction on the out-of -plane flexural behavior of CHS connections. Engineering structures 2021; 231,111711 https://doi.org/10.1016/j. engstruct.2020.111711.

[11] Xue L. Stress based fracture envelope for damage plastic solids. Eng. Fract. Mech.2009; 76: 419-438. https://doi.org/ 10.1016/j.engfracmech.2008.11.010.

[12] Huang XW, Ge JZ, Zhao J, Zhao W. A continuous damage model of Q690D steel considering the influenc-e of Lode parameter and its application. Constr. Build. Mater. 2020; 262: 120067. https://doi.org/10.1016/j.c onbuildmat.2020.120067.

[13] Liu Y, Kang L, Ge H. Experimental and numerical study on ductile fracture of structural steels under different stress states. Constr. Steel. Res.2019; 158: 381-404. https://doi.org/ 10.1016/j.jcsr.2019.04.001.

[14] Xia YS, Huang ZH, Shi XL. Forecast of weld ductility fracture and analysis of Lode angle parameters based on micro-mechanism of round steel X-type tubular joint. Spat. Struct. 2020; 26: 75-82. https://doi.org/ 10.13849/j.issn.1006-6578.2020.04.075. (in Chinese).

[15] Wang YZ, Li GQ, Wang YB, Lyu YF, Li H. Ductile fracture of high strength steel under multi-axial loading. Eng. Struct. 2020; 210: 110401. https://doi.org/ 10.1016/j.engstruct.2020.110401.

[16] Ma XX, Chen YY, Wang W, Qian XD. Weld fracture under non-uniform stress distribution and its mechani

smin CHS-CHS X-joints. Constr. Steel. Res. 2019; 162: 105740. https://doi.org/10.1016/j.jcsr.2019.105740.
[17] Kubík P, Šebek F, Hůlka J, Petruška J. Calibration of ductile fracture criteria at negative stress triaxiality. M ech. Sci. 2016; 108: 90-103. https://doi.org/10.1016/ 10.1016/j.ijmecsci.2016.02.001.
[18] Donghyuk C, Jang YC, Lee Y. Evaluation of the prediction ability of ductile fracture criteria over a wide range of drawing conditions. Mech. Sci. Technol. 2019; 33(9): 4245-4254. https://doi.org/10.1007 /s12206-019-0821-0.
[19] Ma XX, Wang W, Chen YY, Qian XD. Simulation of ductile fracture in welded tubular connections using a simplified damage plasticity model considering the effect of stress triaxiality and lode angle. Constr. Steel Res. 2015; 114: 217-236. https://doi.org/10.1016/j.jcsr.2015.07.023.
[20] Wang W, Liao FF, Chen YY. Ductile fracture prediction and post- fracture path tracing of steel connections based on micromechanics-based fracture criteria. Eng. Mech.2014; 31: 101-108+115.
[21] Han H, Zhen T, Wang XD, Huang ZH. Fracture prediction and bearing capacity analysis of weld of orthogonal CHS X-joints. Building Structure 2022; 53: 99-105. https://doi.org/10.19701/j.jzjg.20211180. (in Chinese).
[22] CECS 280: 2010, Technical specification for structures with steel hollow sections[S]. Beijing: China Planning Press, 2010. (in Chinese).
[23] GB 50661-2011, Code for welding of steel structures[S]. Beijing: China Architecture & Building Press, 2012. (in Chinese).
[24] GB 50017-2017, Standard for Design of Steel Structures[S]. Beijing: China Architecture & Building Press, 2017. (in Chinese).
[25] Chen AG, Wang KM, Xing JH, Chen Y. Ductile fracture behavior of weld metal for Q345 steel under monotonic loading. Eng. Mech.2020, 37(1), 88-97. (in Chinese).
[26] Wardenier, J. Hollow Sections in Structural Applications. Bouwen met Staal, The Netherlands, 2002; 73-77.